ADVANCED MATERIALS
www.advmat.de

Atomic Displacements Enabling the Observation of the Anomalous Hall Effect in a Non-Collinear Antiferromagnet

*Berthold H. Rimmler, Binoy K. Hazra, Banabir Pal, Katayoon Mohseni, James M. Taylor, Amilcar Bedoya-Pinto, Hakan Deniz, Malleswararao Tangi, Ilya Kostanovskiy, Chen Luo, Robin R. Neumann, Arthur Ernst, Florin Radu, Ingrid Mertig, Holger L. Meyerheim, and Stuart S. P. Parkin**

Antiferromagnets with non-collinear spin structures display various properties that make them attractive for spintronic devices. Some of the most interesting examples are an anomalous Hall effect despite negligible magnetization and a spin Hall effect with unusual spin polarization directions. However, these effects can only be observed when the sample is set predominantly into a single antiferromagnetic domain state. This can only be achieved when the compensated spin structure is perturbed and displays weak moments due to spin canting that allows for external domain control. In thin films of cubic non-collinear antiferromagnets, this imbalance is previously assumed to require tetragonal distortions induced by substrate strain. Here, it is shown that in Mn_3SnN and Mn_3GaN, spin canting is due to structural symmetry lowering induced by large displacements of the magnetic manganese atoms away from high-symmetry positions. These displacements remain hidden in X-ray diffraction when only probing the lattice metric and require measurement of a large set of scattering vectors to resolve the local atomic positions. In Mn_3SnN, the induced net moments enable the observation of the anomalous Hall effect with an unusual temperature dependence, which is conjectured to result from a bulk-like temperature-dependent coherent spin rotation within the kagome plane.

1. Introduction

Non-collinear antiferromagnets (NCAFs) can display combinations of intrinsic transport effects that are not usually observed in collinear antiferromagnets or ferromagnets. For instance, NCAFs can display the anomalous Hall effect (AHE) despite having negligible magnetization, which is due to non-zero Berry curvature of the electronic bands.[1–6] Another unexpected effect is the spin Hall effect (SHE), in which spin currents flow transverse to an applied electric field.[7–9] In NCAFs, the spin polarization direction of these spin currents is not restricted to be perpendicular to the charge and spin current directions but can have components in the x- and z-direction.[10–13] This property distinguishes NCAFs from heavy metals such as Pt or W and renders them interesting for spin-orbitronic applications, as it allows for field-free switching of ferromagnetic layers with perpendicular magnetic anisotropy in novel high-density memory devices.[12,14–16]

Such intrinsic transport effects are observed in Mn-based compounds such as Mn_3Z and Mn_3ZN, which are composed of stacked layers of Mn_3Z, where Z are (post-)transition metal atoms. Within these layers, the Mn atoms form trigonal arrangements known as kagome lattices, on which the antiferromagnetically coupled spins are frustrated. This results in the formation of coplanar, non-collinear antiferromagnetic (NCAF) spin textures,[17–19] as shown in **Figure 1**a,b. The magnetic symmetry in these materials allows for finite Berry curvature of the electronic

B. H. Rimmler, B. K. Hazra, B. Pal, K. Mohseni, A. Bedoya-Pinto, H. Deniz, M. Tangi, I. Kostanovskiy, H. L. Meyerheim, S. S. P. Parkin
Max-Planck-Institut für Mikrostrukturphysik
Weinberg 2, 06120 Halle (Saale), Germany
E-mail: stuart.parkin@mpi-halle.mpg.de

J. M. Taylor, C. Luo, F. Radu
Helmholtz-Zentrum Berlin für Materialien und Energie
Hahn-Meitner-Platz 1, 14109 Berlin, Germany

J. M. Taylor, C. Luo
Technische Universität München
Arcisstraße 21, 80333 München, Germany

A. Bedoya-Pinto
Instituto de Ciencia Molecular
Universitat de Valéncia
Av. de Blasco Ibáñez, 13, Paterna 46010, Spain

R. R. Neumann, I. Mertig
Martin-Luther-Universität Halle-Wittenberg
Universitätsplatz 10, 06108 Halle (Saale), Germany

A. Ernst
Johannes Kepler Universität Linz
Altenberger Str. 69, Linz 4040, Austria

The ORCID identification number(s) for the author(s) of this article can be found under https://doi.org/10.1002/adma.202209616

© 2023 The Authors. Advanced Materials published by Wiley-VCH GmbH. This is an open access article under the terms of the Creative Commons Attribution License, which permits use, distribution and reproduction in any medium, provided the original work is properly cited.

DOI: 10.1002/adma.202209616

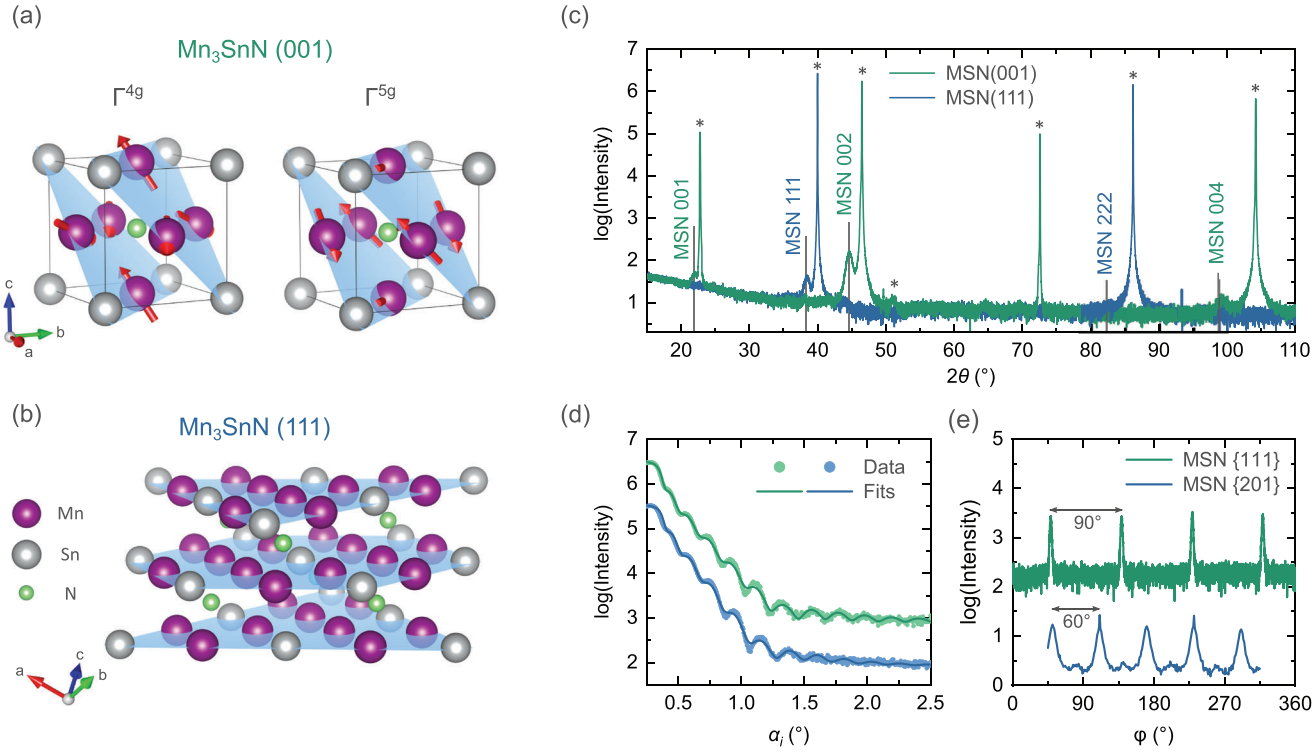

Figure 1. a,b) Graphical representations of the crystal structure of bulk Mn_3SnN in (001)- and (111)-orientation. The (111) kagome planes are shaded in blue. In (a), the non-collinear spin textures corresponding to the irreducible representations Γ^{4g} and Γ^{5g} are shown. c–e) Results from standard structural characterization of 20 nm-thin Mn_3SnN films at room temperature. c) Specular θ–2θ diffraction patterns. Asterisks indicate $SrTiO_3$ reflections and gray lines indicate angular positions of Mn_3SnN bulk reflections. d) XRR scans: specular reflectivity versus incidence angle, α_i. e) Transverse φ-scans of MSN {111} peaks of the (001)-oriented sample and MSN {201} peaks of the (111) -oriented sample.

bands, resulting in an intrinsic AHE.[2–4,20,21] While the hexagonal non-nitride compounds Mn_3Sn and Mn_3Ge have been studied extensively,[22–25] the cubic compounds Mn_3Pt and Mn_3Ir[26,27] as well as the nitrides of type Mn_3ZN (Z = Ni, Ga, Sn)[12,28,29] with antiperovskite structure have attracted much less attention.

Similar to ferromagnets, the measurement of a net anomalous Hall conductivity (AHC) in NCAFs requires an imbalance of the volume fraction of the antiferromagnetic domains. In the hexagonal compounds, Mn_3Ge and Mn_3Sn, single Mn ion anisotropy induces a weak in-plane canted moment that allows for domain structure control by magnetic field.[22] In the cubic systems, an additional mechanism is required to generate spin canting, which, so far, has been attributed to substrate induced tetragonal lattice strain of the epitaxial thin films.[26,28,29] Such tetragonal distortions are a possible mechanism to release the stress exerted on the film by the lattice mismatch between film and substrate.[30] When the lattice is tetragonally elongated or contracted, the interatomic distances between the Mn atoms within the kagome plane become inequivalent. As a result, the antiferromagnetically coupled spins are not exactly compensated, resulting in a net moment coupled to the triangular spin structure.[31–33] This uncompensated moment enables domain structure control and, thereby, allows for the observation of the AHE.

In this work, we show that the AHE can be finite in thin films of the antiperovskite nitride Mn_3SnN (MSN), despite the fact the film structure has a cubic metric within the experimental uncertainty of the measurement. We show that the observation of the AHE in MSN is enabled by so far unexplored displacements of the Mn atoms out of high-symmetry positions. These displacements significantly lower the symmetry of the kagome arrangement and induce spin canting of the otherwise fully compensated NCAF spin texture. This gives rise to local net moments that allow for domain structure control and the observation of the AHE. We also find Mn displacements in Mn_3GaN (MGN) thin films grown by molecular beam epitaxy (MBE). This indicates that Mn displacements and the corresponding symmetry lowering are a general feature of certain antiperovskite nitrides and may, furthermore, be involved in the experimental observation of other intrinsic transport effects.

2. Results and Discussion

2.1. Growth of Mn_3SnN Thin Films

First, we show that thin films of the antiperovskite nitride Mn_3SnN appear as cubic in standard thin film characterization by XRD. MSN thin films were grown on (001)- and (111)-oriented $SrTiO_3$ (STO) substrates by magnetron sputtering. The film composition was varied until a composition close to Mn_3SnN was obtained, as determined by Rutherford backscattering spectroscopy. Structural characterization of the films, shown in Figure 1c–e, shows that MSN grows epitaxially on STO in both growth orientations. For the (001)-oriented film, the angular positions of the out-of-plane film peaks in the θ–2θ scans correspond to those in

© 2023 The Authors. Advanced Materials published by Wiley-VCH GmbH

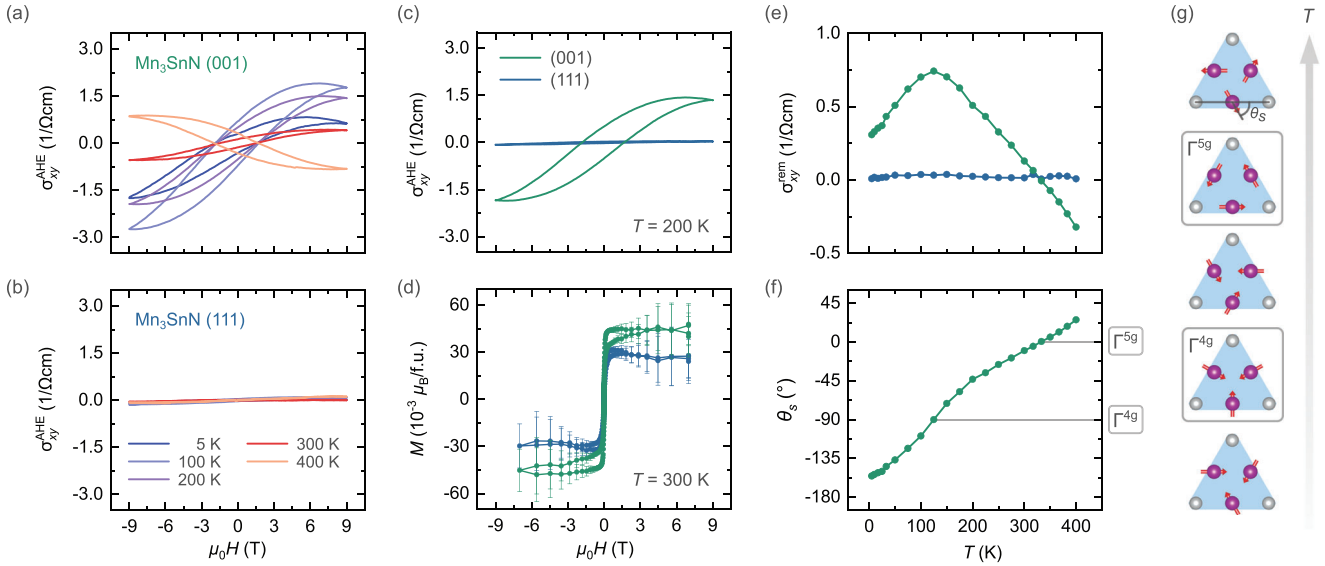

Figure 2. a,b) Anomalous Hall conductivity (AHC) loops of 20 nm-thin (001)- and (111)-oriented Mn_3SnN at various temperatures. c,d) AHC loops at 200 K and magnetic hysteresis loops at 300 K. e) Temperature dependence of the remanent AHC, σ_{xy}^{rem}, after application of +9 *T*. f,g) Calculated in-kagome-plane spin angle, θ_s, versus temperature and graphical representations of the corresponding spin textures viewed along [111].

bulk samples within an experimental uncertainty in 2θ of 0.2°. Transverse φ-scans of the {201} reflections show that the (001)-oriented film grows with cube-on-cube epitaxial relation on STO. The (111)-oriented film shows twinned grains mutually related by 60° rotation around [111] and a minority of grains rotated by 30°. From X-ray reflectivity (XRR) scans as well as from atomic force microscopy and transmission electron microscopy images (see Note S1, Supporting Information) we find that both films grow smoothly on STO with sub-nanometre root mean squared roughness.

In conventional thin films XRD characterization, the lattice parameters and angles are used as the defining characteristic for the crystal symmetry. A film is considered cubic rather than tetragonal, if the lattice parameters are $a = b = c$. Using the six-circle diffractometer, we find that the lattice parameters of our (001)-oriented MSN film are indeed $a = b = c = (4.06 \pm 0.01)$ Å, which corresponds to a tetragonality of $c/a = 1.000 \pm 0.003$. Given the large lattice mismatch of STO and MSN of 3.9%, this value is remarkably close to 1, which corresponds to a perfectly cubic crystal. Based on this simple characterization, zero AHC is expected in this film, which contradicts our measurements, as described in the next section. This discrepancy is resolved by our observation of atomic Mn displacements that reduce the crystal symmetry to tetragonal, without significantly affecting the lattice parameters. Thereby, they remain hidden when only probing the lattice metric.

2.2. Anomalous Hall Effect in Mn_3SnN

Hall effect measurements were carried out using Hall bar devices patterned onto the differently oriented, 20 nm-thin MSN films. We find hole-type charge carriers with a temperature-dependent charge carrier concentration (see Note S2, Supporting Information). The AHC loops in **Figure 2**a,b shows that a non-zero AHE is observed only in the (001)-oriented sample. The linear ordinary Hall and hysteretic anomalous Hall contributions are separated by linear interpolation at high fields.

Zero AHC was previously observed in structurally related Mn_3Ir thin films with (111)-orientation.[27] From symmetry arguments, the AHE is expected to be at a maximum in this measurement configuration.[21] However, the AHE contributions of different NCAF domains related by a spin rotation within the kagome plane of 180° exactly cancel, as the Berry curvature and, therefore, the AHC are odd under time reversal.[2] The AHE vanishes in (111)-oriented MSN, as a magnetic field perpendicular to the kagome planes cannot control the NCAF domain structure. These results also show that potential spin canting out of the (111) plane does not contribute to the hysteretic AHC in either growth orientation.

For the (001)-oriented MSN films, we exclude magnetization as a main contributor to the AHC by comparing magnetotransport and magnetization measurements of the two films. In Figure 2c,d, we plot AHC hysteresis and magnetic hysteresis loops. We find that the magnetization in the two 20 nm-thin films is very low (of the order of magnitude of tens of $m\mu_B$/f.u.), which we confirm by X-ray circular magnetic dichroism (XMCD) measurements (see Note S3, Supporting Information). If a magnetization of this magnitude were sufficient to cause the AHC observed in the (001)-oriented sample, an AHC of similar magnitude would also be expected in the (111)-oriented sample, which is not observed. Furthermore, in a typical ferromagnet, in which the AHC is proportional to the magnetization, the hysteresis loops of magnetization and AHC exhibit the same shape and coercivity. Again, this is not the case in the (001)-oriented sample. Therefore, we conclude that the AHE is not related to the sample magnetization.

As can be seen in Figure 2a, the AHE in (001)-oriented MSN is strongly temperature-dependent. In Figure 2e, we plot the

© 2023 The Authors. Advanced Materials published by Wiley-VCH GmbH

remanent AHC, $\sigma_{xy}^{\mathrm{rem}}$, versus temperature. We find that the AHC of the (001)-oriented sample varies continuously with temperature. This indicates that there are no magnetic phase transition in our MSN thin films, which is supported by our XRD and magnetization measurements. This is unexpected, because bulk MSN shows a complex phase diagram, according to powder neutron diffraction measurements.[19,34] Between T_{N} = 475 and 357 K, bulk MSN is collinear antiferromagnetic and between 357 and 237 K it is non-collinear antiferromagnetic. At lower temperatures, complex ferroic phases with significant magnetization are observed. We conclude that the NCAF phase is stabilized in MSN thin films with (001)- and (111)-orientation. We infer the presence of NCAF order in our MSN samples from magnetic and transport measurements. The NCAF structure can also be measured directly by neutron diffraction, as has been done recently for Mn_3GaN thin films and which confirmed the presence of NCAF order corresponding to the Γ^{5g} configuration at all temperatures in this material also in thin film form.[12]

To resolve the unusual temperature dependence of the AHC in (001)-oriented MSN, we consider that bulk MSN displays spin rotation within the kagome plane as a function of temperature, as found by powder neutron diffraction experiments.[34] The spins retain an angle of 120° with respect to each other, but rotate coherently within the kagome plane. There are two high-symmetry configurations with magnetic space group symmetry $R\bar{3}m'$ (Γ^{4g} irreducible representation) and $R\bar{3}m$ (Γ^{5g}), as shown in Figure 1a. They are characterized by an in-kagome-plane spin angle with respect to the [1−10] direction, θ_{s}, of 90° (or 270°) and 0° (or 180°), respectively. Magnetic textures with other in-kagome-plane angles can be described as a combination of the two irreducible representations and have magnetic space group symmetry $R\bar{3}$. The magnitude and sign of the intrinsic AHC depend on the magnetic symmetry of the spin texture. The AHC is at a maximum in the Γ^{4g} configuration and zero in the Γ^{5g} configuration. Between these two configuration, the AHC depends roughly sinusoidally on θ_{s}.[20,21]

We expect the temperature-dependent spin rotation to manifest in a temperature dependence of the AHC. Therefore, we calculate $\theta_{\mathrm{s}}(T)$ from the measured remanent AHC as:

$$\theta_{\mathrm{s}}(T) = \arcsin\left(\frac{\sigma_{xy}^{\mathrm{rem}}}{\sigma_{xy}^{\mathrm{rem,max}}}\right) \tag{1}$$

We implicitly assume that the observed AHE is of intrinsic origin and that its temperature dependence is dominated by spin rotation. The temperature dependence of the calculated spin angle is plotted in Figure 2f and graphical representations of the corresponding spin textures are presented in Figure 2g. We find that θ_{s} varies continuously and roughly linearly with temperature, in agreement with powder neutron diffraction measurements of bulk MSN.[34] A temperature dependence of the AHC similar to our results was found previously in (001)-oriented MSN thin films.[29] However, only data between 50 and 300 K was reported and the temperature dependence of the AHC not discussed in terms of temperature-dependent spin rotation.

Within our model, we find that spin rotation occurs in a wide range of θ_{s}. This may be due to the NCAF phase being stabilized in the entire temperature range from 4 to 400 K, compared to approximately 120 K in bulk MSN. The spins rotate from $\theta_{\mathrm{s}} \approx$ 45° at the highest measurement temperature of 400 K toward the Γ^{5g} at the temperature with zero AHC of 330 K. They then rotate further toward Γ^{4g} at 125 K and further at lower temperatures. In bulk MSN, spin rotation occurs only from 90° to 45°.[34] Phenomenologically, spin rotation in antiperovskite nitrides can be explained on the basis of temperature-dependent magnetocrystalline anisotropy.[35] In bulk MSN this temperature-dependent anisotropy is due to small changes in the lattice constants with varying temperature. The case is likely more complex in MSN thin films, in which constrictions imposed by the substrate have to be considered. Furthermore, as will be discussed in the next section, there are displacements of the Mn atoms, which may further affect the temperature dependence of the magnetic anisotropy. Nevertheless, the fact that the remanent AHC in our (001)-oriented MSN thin films can be modelled based on an in-kagome-plane spin angle varying linearly with temperature provides further evidence for the an intrinsic AHE in our MSN thin films.

2.3. Atomic Manganese Displacements

The observation of the AHE in the (001)-oriented film is unexpected, as the lattice parameters suggests cubic crystal symmetry. To resolve this discrepancy, we have carried out quantitative XRD experiments using a six-circle diffractometer and a highly brilliant X-ray beam under grazing incidence. The integrated intensities of a set of symmetry-inequivalent reflection are measured and several structural models fitted to the measured intensities. The unweighted residual, R_{u}, calculated based on the squared structure factor amplitudes is used as a measure for the fit quality (see Experimental Section).

First, the bulk cubic structure of MSN with space group (SGR) $Pm\bar{3}m$ (Nr. 221) is considered, including isotropic disorder at all atomic sites. In this case, R_{u} is equal to 16% (see also Table S2, Supporting Information). Given the simple atomic structure with no free positional parameters, this represents a quite high value and suggests that the film structure is considerably more complicated than that of bulk MSN.

Therefore, we modify the structural model by reducing the symmetry to the tetragonal SGR $P4mm$ (Nr. 99), in which the Mn atomic sites located at the centres of the {001} and {100} faces are inequivalent. Furthermore, we include anisotropic anharmonic structural disorder, which is described by anharmonic displacements parameters (ADPs) with tensor components of third order (C^{klm}) and forth order (D^{klmn}).[36] The SGR $P4mm$ is a non-isomorphic subgroup of SGR $P4/mmm$ (Nr. 123), which itself is a subgroup of $Pm\bar{3}m$. This drastic symmetry lowering is justified in the context of the observation of the AHE, as discussed below. In SGR $P4mm$, the Wyckoff sites of the symmetry-inequivalent Mn atoms are 1b ($\frac{1}{2}$, $\frac{1}{2}$, z) and 2c (0, $\frac{1}{2}$, z). The point group symmetry at these sites, which determine which ADP tensor coefficients can be non-zero, is $4mm$ and $mm2$, respectively. The number of fit parameters is reduced by symmetry constraints where certain tensor components become zero (exemplary values presented in Table S3, Supporting Information). Refinement of this ADP model yields a considerable improvement of the fit quality to R_{u} = 0.02%.

© 2023 The Authors. Advanced Materials published by Wiley-VCH GmbH

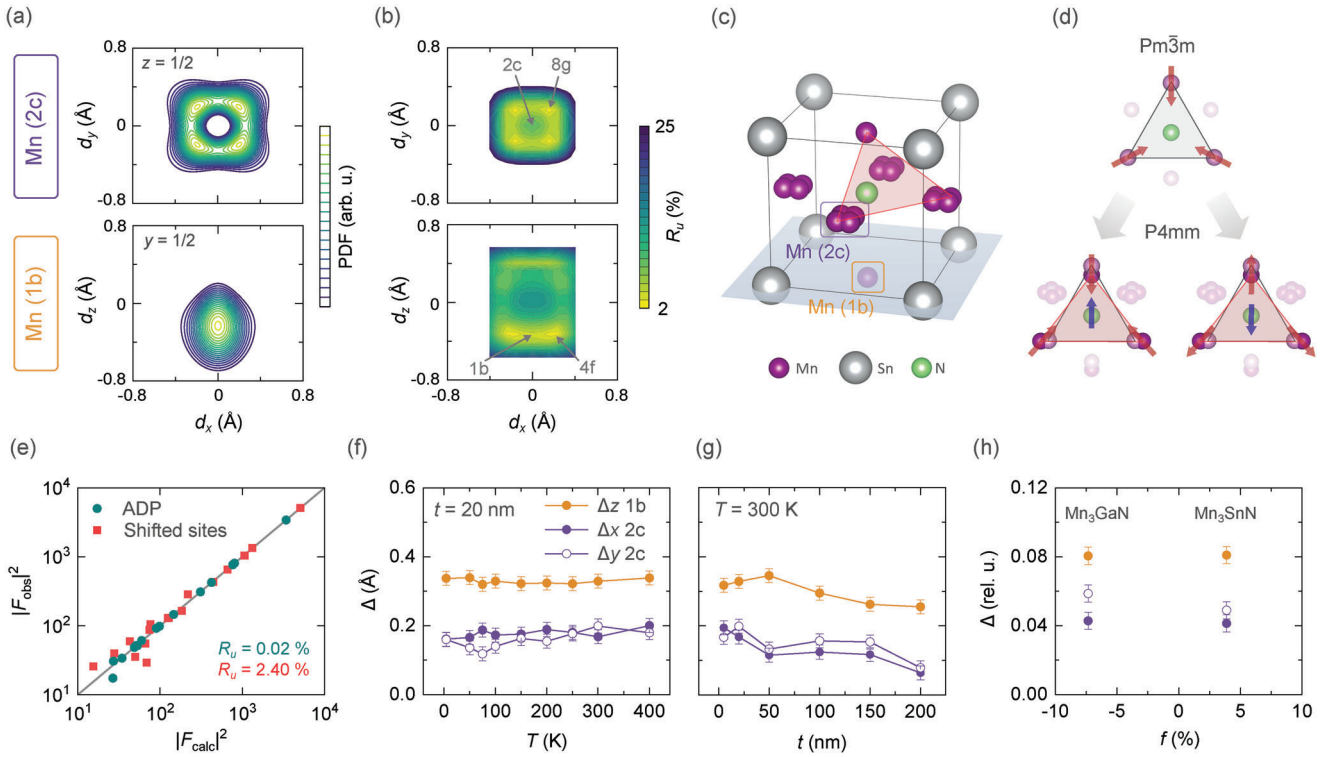

Figure 3. a,b) XRD refinement of two structural models for 20 nm (001)-oriented Mn_3SnN measured at 300 K. a) Atomic-displacement parameter (ADP) model: sections of the probability density function (PDF) at the Wyckoff positions 2c and 1b (in space group *P4mm*). b) Shifted-sites model: contour plots of the unweighted residual, R_u, versus atomic positions of the sites 8g (near 2c) and 4f (near 1b). c) Crystal structure of Mn_3SnN thin films with Mn displacements (atomic radii reduced for clarity). d) Simplified views of the crystal structure along the [111] direction with and without Mn displacements. Mn atoms at high-symmetry positions shown in light magenta and certain atoms omitted. The red and blue arrows represent the atomic Mn moments and the resulting net moment. e) Plot of observed versus calculated squared structure factor amplitudes for the two models. f,g) Temperature and film-thickness dependences of the magnitude of Mn displacements in the shifted-sites model. h) Displacement magnitude calculated using the shifted-sites model in relative lattice units versus lattice mismatch of Mn_3SnN on $SrTiO_3$ (R_u = 2.4%) and Mn_3GaN on MgO (R_u = 2.9%).

Real space representation of the atomic disorder is provided by the probability density function (PDF), which is the Fourier transform of the generalized Debye-Waller factor which includes higher-order anharmonic corrections.[36] Sections of the PDFs at the atomic sites 2c and 1b are shown in **Figure 3**a. Here, d_i ($i = x, y, z$) describe spatial coordinates with respect to the face centres $(\frac{1}{2}, 0, \frac{1}{2})$ and $(\frac{1}{2}, \frac{1}{2}, 0)$. Both sites exhibit strongly anisotropic disorder deviating from the ellipsoidal shape expected from a purely harmonic description. At the 2c site, four distinct maxima of the PDF in the (001) plane are observed, while at the 1b site, the maximum of the PDF lies at $d_z = -0.25$ Å. The PDFs at the two sites can be interpreted to reflect Mn atoms that are shifted away from the high-symmetry, face-centred positions.

This is confirmed by employing an alternative approach, in which the disorder is treated by purely harmonic displacement parameters but the atomic positions are allowed to vary. In the vicinity of the 2c site, the Mn position is split into four symmetry-equivalent sites corresponding to the Wyckoff position 8g $(x, y, \frac{1}{2})$, each occupied with a probability of 1/4. In the case of the 1b position, the *x*- and the *z*-positions are varied (now site 4f). In Figure 3b, we show contour plots of the residual R_u as a function of the 8g and 4f site positions. In agreement with the ADP model, the 2c site is split into four 8g sites that fall into distinct minima of R_u in the vicinity of 2c. Similarly, the *z*-position of the 4f site atom is shifted to $d_z = -0.35$ Å. The lowest R_u that can be achieved in this shifted-sites model is 2.4%. We find that the ADP and the shifted-sites model yield low residuals and are in very good agreement with each other.

A schematic representation of the structure with displaced Mn atoms is shown in Figure 3c, highlighting the multi-modal splitting of the 2c site and the shift of the Mn atom at the 1b site toward lower *z* values. The shifted-sites model suggests that the vacancy between the displaced Mn atom and the N atom may be occupied by a minority of Mn atoms shifted to positive d_z. For simplicity, we consider only a single displaced Mn atom at the 1b site, which is, furthermore, not split in the *x*-*y*-plane. The Mn displacements found here have to be distinguished from tetragonal distortions considered in previous work, which are characterized by a global change in lattice constants, such that $a = b \neq c$. In contrast, the symmetry lowering by Mn displacements does not manifest in a modification of the lattice parameters, which are found to be $a = b = c = (4.06 \pm 0.01)$ Å. Instead, it is observed by determining the exact atomic positions.

The shifted-sites model can also be used to quantify the magnitude of the Mn displacements at the two sites as a function of temperature and film thickness, as plotted in Figure 3f,g. At both sites, the shift away from the high-symmetry points increases slightly with increasing temperature, which can be attributed to

© 2023 The Authors. Advanced Materials published by Wiley-VCH GmbH

thermal disorder. By varying the film thickness, we find that the Mn displacements generally decrease with increasing film thickness. This is expected, since the film crystal structure converges toward that of the bulk in the limit of high thickness (linear extrapolation yields a thickness in the range of approximately 0.4 µm to 0.6 µm). Since the lattice mismatch of STO and MSN is quite large (3.9%), the reason for the formation of Mn displacement is possibly relaxation of the resulting stress. Interestingly, the maximum displacement in z of the 1b site Mn atom is observed for a thickness of 50 nm. This may be due to an accumulation of stress up to a certain film thickness, above which the formation of misfit dislocations is favoured.

2.4. Manganese Displacements and the Anomalous Hall Effect in Mn_3SnN

We resolve the discrepancy between the films appearing cubic from standard XRD analysis and the presence of non-zero AHE by considering the effect of atomic Mn displacements on the NCAF structure. Antiperovskite nitrides display strong magnetostructural coupling effects.[32,33,37–40] Even small changes in the crystal structure may entail drastic changes in the magnetic structure. In the presence of displacements, the triangular arrangements of Mn atoms in the [111] kagome plane are highly distorted. In Figure 3d, we show the crystal structure of MSN with Mn displacements viewed along the [111] direction for the cubic case and for a possible case with Mn displacements. In the bulk case (SGR $Pm\bar{3}m$), the Mn atoms occupy high-symmetry sites and form equilateral triangles that lie within the kagome plane (shown in grey). In the presence of Mn displacements (SGR $P4mm$), the bond lengths and angles between the Mn atoms vary locally (red triangles). As a result, the moments slightly cant away from the compensated 120° spin texture, thus giving rise to a net moment. This is shown schematically for two magnetic domains related by a spin rotation by 180° assuming a magnetic configuration that correspond to a distorted Γ^{4g} configuration. We have carried out ab initio calculations based on exemplary model structures to investigate how displacements at the different sites affect the local spin configuration (Note S5, Supporting Information). Indeed, we find that Mn displacements, specifically those at the 1b site, cause canting by several degrees within the kagome plane, which leads to the emergence of small net moments.

The observation of a non-zero AHE justifies the symmetry lowering from SGR $Pm\bar{3}m$ to $P4mm$ in our structural refinement. A highest-order non-isomorphic subgroup of $Pm\bar{3}m$ is $P4/mmm$. However, this SGR is characterized by inversion symmetry. As a result, the local canted moments induced by the symmetrically displaced Mn atoms cancel out on average. Therefore, the model is insufficient to explain the observation of the AHE. In the case of the SGR $P4mm$, which is itself a highest-order non-isomorphic subgroup of $P4/mmm$, inversion symmetry is broken and the 1b site atoms are displaced asymmetrically along the z-axis, leading to a globally acentric structure. Therefore, application of a magnetic field along the z-direction selectively favours certain magnetic domains, thus resulting in a hysteretic AHE, as sketched in Figure 3d. Furthermore, structural refinement assuming SGR $P4mm$ and using third- and fourth-order ADPs yields a significantly better fit than SGR $P4/mmm$ (R_u = 0.02%, compared to 0.6%).

In summary, structural analysis of thin films providing only lattice parameters are not able to disentangle the subtle details of atomic disorder, which requires the precise analysis of a large data set covering a wide range of scattering vectors in reciprocal space. Therefore, in previous work, tetragonal strain was assumed to be the only mechanism allowing for domain control.[12,26,28,29] We show that non-zero transport properties arising from the NCAF structure can be related, instead, to more subtle details of the film structure, namely atomic displacements of Mn, which leads to a symmetry lowering from cubic ($Pm\bar{3}m$) to tetragonal ($P4mm$), without affecting the lattice parameters within the measurement resolution.

An open question is the effect of Mn displacements on the temperature-dependent spin rotation. The linear dependence of the calculated spin rotation angle θ_s on temperature suggests that, in first approximation, Mn displacements do not affect the spin rotation. Instead, they only enable measurement of the AHE through spin canting of the otherwise fully compensated NCAF spin texture. This is warranted by the fact that the evolution of the Mn displacements with temperature is small and continuous, as seen from Figure 3f. Nevertheless, as discussed above, magnetocrystalline anisotropy is highly sensitive to small changes in the crystal structure. Therefore, it cannot be excluded that the Mn displacements affect the magnetocrystalline anisotropy and, thereby, the spin rotation through structural modifications that are not detected. This may explain the differences in the details of the temperature-dependent spin rotation between bulk material and thin films.

2.5. Manganese Displacements in Other Non-Collinear Antiferromagnets

Our observation of structural symmetry lowering and its role in enabling the observation of the AHE in MSN is also relevant for the observation of the spin Hall effect (SHE) in the cubic NCAFs Mn_3GaN (MGN) and MSN.[12,41] In contrast to heavy metals, the spin polarization direction is not restricted to be perpendicular to the charge and spin current directions. Instead, polarization components in the x- and z-direction are also allowed.[10–13] However, similar to the AHE, the presence of certain antiferromagnetic domains can lead to a cancellation of the effect. Since the SHE is even under time reversal symmetry, domains related by a spin rotation by 180° are irrelevant. Rather, one has to consider different domains that result from a lattice rotation by 90° around the z-axis. An imbalance of these domains is required for the spin polarization components in the x- and z-direction to be observed.[12] However, the MGN films studied by spin-torque ferromagnetic resonance in ref. [12] display only a small tetragonal distortion of $c/a = 0.996$, indicating that they are mostly cubic, similar to our MSN films. We propose that the SHE in MGN is enabled not by tetragonal distortion but, rather, by atomic Mn displacements.

To test this possibility, we have grown a 25 nm-thin Mn_3GaN film by MBE on (001)-oriented MgO. We perform structural analysis and find significant Mn displacements also in this antiperovskite. We obtain a good fit of the data using the shifted-sites model established for MSN (R_u = 2.9%). In Figure 3h, we plot

© 2023 The Authors. Advanced Materials published by Wiley-VCH GmbH

the displacement magnitudes of the different sites as a function of the lattice mismatch of film (f) and substrate (s), $f = (a_f - a_s)/a_s$, and find that, within the margin of error, the magnitudes of the Mn displacements are similar in the two antiperovskites. This shows that Mn displacements are formed under compressive strain (MSN) as well as under tensile (MGN) strain. Furthermore, it shows that the formation of Mn displacements is not limited to a single material or deposition technique.

Non-collinear antiferromagnetism is also found in cubic nonnitride compounds Mn_3Z (Z = Ir, Pt), which are structurally similar to the antiperovskites discussed here. Accordingly, tetragonal distortion was also assumed as the extrinsic mechanism allowing for domain control in Mn_3Pt.[26] Whether Mn displacements are also present in these materials remains subject of further study. In the hexagonal Mn_3Ge and Mn_3Sn, domain control is enabled by intrinsic spin canting. Nevertheless, structural disorder may affect the transport properties. For instance, topological Hall signatures have been found in Mn_3Sn thin films,[42] which may be induced or enhanced by structural disorder.

3. Conclusion

We have shown that atomic Mn displacements enable the observation of the AHE in the NCAF Mn_3SnN. The formation of these displacements may be a novel mechanism for stress relaxation in Mn-based antiperovskites. It is possible that similar structural symmetry lowering is present in other materials in thin film form, since it is, as we demonstrate here, generally hidden in conventional thin film XRD characterization. Our results also show that the formation of Mn displacements is not limited to a certain material or deposition technique. Beyond the AHE and SHE, Mn displacements may, furthermore, be involved in the measurement of other transport effects that require a domain imbalance, such as the anomalous Nernst effect,[43,44] the magneto-optical Kerr effect[20] as well as longitudinal spin current polarization.[11,13] We show that tetragonal distortions in thin films are not a prerequisite to measuring these effects, but that their observation may be enabled, instead, by atomic displacements.

More generally, one of the main advantages of antiferromagnets for spintronic devices is their insensitivity to magnetic fields. However, this property also makes the control of the antiferromagnetic domain structure far more challenging compared to ferromagnets. The same practical problem may also arise in the newly found class of altermagnets.[45] Elaborate writing and reading schemes can overcome this problem, as has been demonstrated for the collinear antiferromagnets MnCuAs and Mn_2Au.[46,47] However, beyond new device architectures, thin film engineering of structural symmetry lowering induced by atomic displacements may open up new avenues for controlling the domain structure of antiferromagnets, which may allow for direct substitution of ferromagnets by antiferromagnets in spintronic devices with well established device architectures.

4. Experimental Section

Growth: Single-side-polished $SrTiO_3$ (STO) substrates with (001)- and (111)-orientation (Crystec GmbH, Berlin, Germany) were subjected to a cleaning treatment using a buffered hydrofluoric acid solution and subsequent annealing in a tube furnace at 930 °C for 2.5 h under O_2 flow.[48]

Growth of Mn_3SnN thin films was performed in a ultra-high vacuum dc magnetron sputtering system with a base pressure of $<1 \times 10^{-9}$ mbar. Mn_3SnN was grown by co-sputtering from Mn and Sn targets in an Ar/N_2 background atmosphere on (001)- and (111)-oriented STO substrates heated to 500 and 350 °C, respectively. TaN or Pt capping layers were deposited by sputtering from Ta or Pt targets in Ar/N_2 or Ar atmosphere. The chamber pressure was 4×10^{-3} mbar throughout the process. All targets were 99.99% pure. The composition of Mn_3SnN was optimized using Rutherford backscattering spectroscopy (RBS) measurements of samples grown at room temperature on pyrolytic carbon substrates: C/Pt (3 nm)/Mn_3SnN (≈ 25 nm)/Pt (3 nm). The optimized parameters (Mn:Sn sputtering power ratio of 45:8 and Ar:N_2 gas flow ratio of 80:20) yielded samples with stoichiometry $Mn_3Sn_1N_{0.96}$. The typical relative errors are 0.5% for Mn and Sn, and 2% for N. Within the accuracy of the measurement we obtained stoichiometric Mn_3SnN thin films at room temperature.

Growth of Mn_3GaN on MgO(100) substrates was carried out using a *VEECO* Gen 10 radio frequency plasma assisted molecular beam epitaxy (RF-PAMBE) system at a substrate temperature of 500 °C. The MgO substrates were chemically rinsed repeatedly in acetone, methanol, and isopropyl alcohol each for 10 min. Later, the substrates were outgassed in a load lock chamber at 200 °C for 30 min. Further cleaning was accomplished in the growth chamber at 850 °C for 2 h. During growth, a N-plasma source was operated at 4 sccm and 250 W RF power while the Mn and Ga metals were evaporated using dual filament effusion cells. Beam equivalent pressures of Mn and Ga were recorded as 6.1×10^{-8} and 3.3×10^{-8} mbar. All the samples were capped with AlN at room temperature.

Device Fabrication: The MSN thin films were patterned into double Hall crosses using photo-lithography. The patterned devices were etched by Ar ion beam milling. A metallic bilayer consisting of Ti (2 nm)/Au (100 nm) was used for the contacts. A microscopy image of the fabricated Hall bar used in the measurements is shown in Note S2 (Supporting Information).

AFM: Atomic force microscopy (AFM) images were obtained using a Bruker Dimension-Icon AFM.

TEM: An FEI Nova 600 Nanolab focused ion beam (FIB) system was used to prepare thin lamellae from the Mn_3SnN films for high-resolution transmission electron microscopy (TEM) and scanning TEM (STEM) imaging. The cross-sectional lamellae were later characterized using a JEOL JEM-F200 electron microscope equipped with a Schottky-type electron gun and an annular dark-field detector at an accelerating voltage of 200 kV.

Magnetic Characterization: In-house magnetic measurements were performed using a Quantum Design MPMS3 SQUID-VSM. For in-plane measurements, the samples were glued onto a quartz rod. For out-of-plane measurements, the samples were cut into smaller pieces and fixed in a plastic straw. All measurements were performed in VSM mode. The lateral sample dimensions were measured under an optical microscope to be approximately 25 mm^2 for the samples measured in-plane and 13 mm^2 for the sample measured out-of-plane.

Soft-X-ray magnetic circular dichroism (XMCD) measurements were performed in total electron yield mode at the VEKMAG end station at BESSY II, Berlin (Germany).

Transport Measurements: Magnetotransport measurements were performed using a Quantum Design 9 T Physical Properties Measurement System (PPMS). The samples were glued onto standard holders with GE varnish for dc measurements and wire-bonded to contact pads with Al wires. The longitudinal resistivity, ρ_{xx}, was measured in four-probe geometry using the double Hall cross devices. The transverse resistivity was calculated from the transverse resistance R_{xy} and the film thickness t as $\rho_{xy} = R_{xy}t$. The transverse conductivity was calculated as $\sigma_{xy} = -\rho_{xy}/\rho_{xx}^2$. Hall resistivity and conductivity loops presented here are shifted along the ordinate axis to remove effects of sample charging and offset voltages of the nanovoltmeter.

© 2023 The Authors. Advanced Materials published by Wiley-VCH GmbH

XRD and Structural Refinement: A Bruker D8 Discover system equipped with a Cu-K_α anode and a 2D detector by *DECTRIS* was used for X-ray Reflectivity (XRR), out-of-plane $\theta-2\theta$ and φ-scans.

All other X-ray diffraction (XRD) measurements were performed using a custom-made six-circle diffractometer equipped with a gallium-jet X-ray source operated at 70 keV and 100 W electron beam power emitting Ga-K_α radiation ($\lambda = 1.3414$ Å) focused onto the sample by Montel optics providing a highly collimated beam of 100 µm height and 2 mm width. The incidence angle of the beam at the sample was 1°. The six-circle diffractometer was operated in *z*-axis mode.[49] A liquid-helium cryostat equipped with a beryllium dome was used for temperature-dependent XRD measurements.

Integrated intensities, I_{obs}, of 17 symmetry-independent reflections (hkl) were recorded. The observed intensities are proportional to the squares of the structure factor magnitudes: $I_{\text{obs}}(hkl) \propto |F_{\text{obs}}(hkl)|^2$. We consider different structural models and calculate their structure factors:

$$F_{\text{calc}}(\vec{q}) \propto \sum_\alpha f_\alpha \exp\left(-2\pi i \vec{q}\cdot\vec{r_\alpha}\right)\cdot T_\alpha^{\text{H}}(\vec{q}) \tag{2}$$

Herein, $\vec{q}$ is the scattering vector and the sum runs over all atoms α with atomic form factor f_α and position $\vec{r_\alpha}$. T_α^{H} is the Debye–Waller factor, which describes the harmonic (H) disorder:

$$T_\alpha^{\text{H}}(\vec{q}) = \exp\left(-8\pi^2 U_\alpha^{kl} q_k q_l\right) \tag{3}$$

wherein U_α^{kl} ($k,l = 1, 2, 3$) are the mean squared atomic displacement amplitudes and q_k, q_l are the components of $\vec{q}$.

The average relative disagreement of a given model with the experimental data is given by the unweighted residual:

$$R_u = \frac{\sum_{hkl} ||F_{\text{obs}}(hkl)|^2 - |F_{\text{calc}}(hkl)|^2|}{\sum_{hkl} |F_{\text{obs}}(hkl)|^2} \tag{4}$$

Structural refinement is then carried out by least squares fitting to minimize the unweighted residual, R_{u}.[50]

Anharmonic corrections to the Debye–Waller factor were taken into account using a Gram–Chalier (GC) series development up to forth order:[36]

$$T_\alpha^{\text{GC}}(\vec{q}) = T_\alpha^{\text{H}}(\vec{q})\left[1 + \frac{1}{3!}(2\pi i)^3 \cdot q_k q_l q_m \cdot C_\alpha^{klm} + \frac{1}{4!}(2\pi i)^4 \cdot q_k q_l q_m q_n \cdot D_\alpha^{klmn}\right] \tag{5}$$

The term in square brackets describes the deviation from the harmonic Debye–Waller approximation. It includes the anharmonic displacement parameters (ADPs) in the form of tensors of rank three (C_α^{klm}) and four (D_α^{klmn}). The structure factor including anharmonic contributions is then given by:

$$F^{\text{GC}}(\vec{q}) = \sum_\alpha f_\alpha \exp\left(-2\pi i\, \vec{q}\cdot\vec{r_\alpha}\right) T_\alpha^{\text{GC}} \tag{6}$$

Real-space representations of the atomic positions are provided by the probability density function PDF($\vec{u}$), obtained from the Fourier transform of $T_\alpha^{\text{GC}}(\vec{q})$:

$$\text{PDF}^{\text{GC}}(\vec{u}) = \text{PDF}^{\text{H}}(\vec{u})\left[1 + \frac{1}{3!}C^{klm}H_{klm}(\vec{u}) + \frac{1}{4!}D^{klmn}H_{klmn}(\vec{u})\right] \tag{7}$$

$H(\vec{u})$ represents the Hermite polynomials,[51] which are the nth order derivatives of the 3D harmonic PDF to the components u_i of the displacement vector $\vec{u}$. The displacement vector is defined with respect to the position of the atomic site under consideration. In the harmonic approximation, the PDF can be written as a trivariate Gaussian function:

$$\text{PDF}^{\text{H}}(\vec{u}) = \sqrt{\frac{\det(U^{-1})}{(2\pi)^3}} \exp\left(-\frac{1}{2}\vec{u}^T U_\alpha^{-1}\vec{u}\right). \tag{8}$$

Supporting Information

Supporting Information is available from the Wiley Online Library or from the author.

Acknowledgements

B.R. and A.B.-P. thank the HZB for allocation of synchrotron radiation beam time under proposal 212-10661. A.B.-P. acknowledges support by the Generalitat Valenciana (CIDEGENT/2021/005). A.E. acknowledges funding by Fonds zur Förderung der wissenschaftlichen Forschung (FWF) grant I 5384. Calculations were performed at Rechenzentrum Garching of the Max Planck Society (Germany). B.R. greatly appreciates fruitful discussion with Prof. Olena Gomonay.

Open access funding enabled and organized by Projekt DEAL.

Conflict of Interest

The authors declare no conflict of interest.

Author Contributions

Berthold H. Rimmler: Conceptualization; Data Curation; Formal Analysis; Investigation; Methodology; Software; Visualization; Writing – Original – Draft; Writing – Review – Editing; Binoy K. Hazra: Conceptualization; Investigation; Writing – Original – Draft; Writing – Review – Editing; Banabir Pal: Investigation; Writing – Original – Draft; Katayoon Mohseni: Investigation; James M. Taylor: Conceptualization; Supervision; Writing – Review – Editing; Amilcar Bedoya-Pinto: Investigation; Writing – Review – Editing; Hakan Deniz: Investigation; Writing – Original – Draft; Malleswararao Tangi: Investigation; Ilya Kostanovskiy: Investigation; Chen Luo: Investigation; Robin R. Neumann: Methodology; Arthur Ernst: Investigation; Florin Radu: Conceptualization; Supervision; Writing – Review – Editing; Ingrid Mertig: Conceptualization; Supervision Writing – Review – Editing; Holger L. Meyerheim: Investigation; Writing – Original – Draft; Writing – Review – Editing; Stuart S. P. Parkin: Conceptualization; Funding – Acquisition; Methodology; Supervision; Writing – Review – Editing.

Data Availability Statement

The data that support the findings of this study are available from the corresponding author upon reasonable request.

Keywords

anomalous Hall effect, non-collinear antiferromagnets, spin rotation, X-ray diffraction

Received: October 18, 2022
Revised: February 10, 2023
Published online: April 27, 2023

© 2023 The Authors. Advanced Materials published by Wiley-VCH GmbH

[1] N. Nagaosa, J. Sinova, S. Onoda, A. H. MacDonald, N. P. Ong, *Rev. Mod. Phys.* **2010**, *82*, 1539.
[2] D. Xiao, M.-C. Chang, Q. Niu, *Rev. Mod. Phys.* **2010**, *82*, 1959.
[3] H. Chen, Q. Niu, A. MacDonald, *Phys. Rev. Lett.* **2014**, *112*, 017205.
[4] J. Kübler, C. Felser, *Europhys. Lett.* **2014**, *108*, 67001.
[5] V. Baltz, A. Manchon, M. Tsoi, T. Moriyama, T. Ono, Y. Tserkovnyak, *Rev. Mod. Phys.* **2018**, *90*, 015005.
[6] L. Šmejkal, A. H. MacDonald, J. Sinova, S. Nakatsuji, T. Jungwirth, *Nat. Rev. Mater.* **2022**, 1.
[7] J. Sinova, S. O. Valunzela, J. Wunderlich, C. H. Back, T. Jungwirth, *Rev. Mod. Phys.* **2015**, *87*, 1213.
[8] W. Zhang, W. Han, S.-H. Yang, Y. Sun, Y. Zhang, B. Yan, S. S. P. Parkin, *Sci. Adv.* **2016**, *2*, 1600759.
[9] M. Kimata, H. Chen, K. Kondou, S. Sugimoto, P. K. Muduli, M. Ikhlas, Y. Omori, T. Tomita, A. H. MacDonald, S. Nakatsuji, Y. Otani, *Nature* **2019**, *565*, 627.
[10] Y. Zhang, Y. Sun, H. Yang, J. Železný, S. P. P. Parkin, C. Felser, B. Yan, *Phys. Rev. B* **2017**, *95*, 075128.
[11] J. Železný, Y. Zhang, C. Felser, B. Yan, *Phys. Rev. Lett.* **2017**, *119*, 187204.
[12] T. Nan, C. X. Quintela, J. Irwin, G. Gurung, D. F. Shao, J. Gibbons, N. Campbell, K. Song, S.-Y. Choi, L. Guo, R. D. Johnson, P. Manuel, R. V. Chopdekar, I. Hallsteinsen, T. Tybell, P. J. Ryan, J.-W. Kim, Y. Choi, P. G. Radaelli, D. C. Ralph, E. Y. Tsymbal, M. S. Rzchowski, C. B. Eom, *Nat. Commun.* **2020**, *11*, 4671.
[13] G. Gurung, D.-F. Shao, E. Y. Tsymbal, *Phys. Rev. Mater.* **2021**, *5*, 124411.
[14] D. MacNeill, G. M. Stiehl, M. H. D. Guimaraes, R. A. Buhrman, J. Park, D. C. Ralph, *Nat. Phys.* **2017**, *13*, 300.
[15] A. M. Humphries, T. Wang, E. R. J. Edwards, S. R. Allen, J. M. Shaw, H. T. Nembach, J. Q. Xiao, T. J. Silva, X. Fan, *Nat. Commun.* **2017**, *8*, 911.
[16] S.-H. C. Baek, V. P. Amin, Y.-W. Oh, G. Go, S.-J. Lee, G.-H. Lee, K.-J. Kim, M. D. Stiles, B.-G. Park, K.-J. Lee, *Nat. Mater.* **2018**, *17*, 509.
[17] E. Krén, G. Kédér, L. Pél, J. Sólyom, P. Szabó, T. Tarnóczi, *Phys. Rev.* **1968**, *171*, 574.
[18] T. Nagamiya, S. Tomiyoshi, Y. Yamaguchi, *Solid State Commun.* **1982**, *42*, 385.
[19] D. Fruchart, E. F. Bertaut, *J. Phys. Soc. Jpn* **1978**, *44*, 781.
[20] X. Zhou, J.-P. Hanke, W. Feng, F. Li, G.-Y. Guo, Y. Yao, S. Blügel, Y. Mokrousov, *Phys. Rev. B* **2019**, *99*, 104428.
[21] G. Gurung, D.-F. Shao, T. R. Paudel, E. Y. Tsymbal, *Phys. Rev. Mater.* **2019**, *3*, 044409.
[22] S. Nakatsuji, N. Kiyohara, T. Higo, *Nature* **2015**, *527*, 212.
[23] A. K. Nayak, J. E. Fischer, Y. Sun, B. Yan, J. Karel, A. C. Komarek, C. Shekhar, N. Kumar, W. Schnelle, J. Kübler, C. Felser, S. S. P. Parkin, *Sci. Adv.* **2016**, *2*, e1501870.
[24] M. Ikhlas, T. Tomita, T. Koretsune, M.-T. Suzuki, D. Nishio-Hamane, R. Arita, Y. Otani, S. Nakatsuji, *Nat. Phys.* **2017**, *13*, 1085.
[25] C. Wuttke, F. Caglieris, S. Sykora, F. Scaravaggi, A. U. B. Wolter, K. Manna, V. Süss, C. Shekhar, C. Felser, B. Büchner, C. Hess, *Phys. Rev. B* **2019**, *100*, 085111.
[26] Z. Q. Liu, H. Chen, J. M. Wang, J. H. Liu, K. Wang, Z. X. Feng, H. Yan, X. R. Wang, C. B. Jiang, J. M. D. Coey, A. H. MacDonald, *Nat. Electron.* **2018**, *1*, 172.
[27] J. M. Taylor, E. Lesne, A. Markou, F. K. Dejene, P. K. Sivakumar, S. Pöllath, K. G. Rana, N. Kumar, C. Luo, H. Ryll, F. Radu, F. Kronast, P. Werner, C. H. Back, C. Felser, S. S. P. Parkin, *Appl. Phys. Lett.* **2019**, *115*, 062403.
[28] D. Boldrin, I. Samathrakis, J. Zemen, A. Mihai, B. Zou, F. Johnson, B. D. Esser, D. W. McComb, P. K. Petrov, H. Zhang, L. F. Cohen, *Phys. Rev. Mater.* **2019**, *3*, 094409.
[29] Y. You, H. Bai, X. Chen, Y. Zhou, X. Zhou, F. Pan, C. Song, *Appl. Phys. Lett.* **2020**, *117*, 222404.
[30] H. Lüth, *Solid Surfaces, Interfaces and Thin Films*, Graduate Texts in Physics. Springer, Heidelberg, 5th Ed., **2010**.
[31] P. Lukashev, R. F. Sabirianov, *J. Appl. Phys.* **2010**, *107*, 09E115.
[32] J. Zemen, E. Mendive-Tapia, Z. Gercsi, R. Banerjee, J. B. Staunton, K. G. Sandeman, *Phys. Rev. B* **2017**, *95*, 184438.
[33] J. Zemen, Z. Gercsi, K. G. Sandeman, *Phys. Rev. B* **2017**, *96*, 024451.
[34] D. Fruchart, E. F. Bertaut, J. P. Sénateur, R. Fruchart, *J. Phys. Lett.* **1977**, *38*, 21.
[35] E. V. Gomonaj, V. A. L'vov, *Phase Transitions* **1992**, *38*, 15.
[36] W. F. Kuhs, *Acta Crystallogr., Sect. A: Found. Crystallogr.* **1992**, *48*, 80.
[37] E. V. Gomonaj, *Phase Transitions* **1989**, *18*, 93.
[38] P. Lukashev, R. F. Sabirianov, K. Belashchenko, *Phys. Rev. B* **2008**, *78*, 184414.
[39] K. Takenaka, M. Ichigo, T. Hamada, A. Ozawa, T. Shibayama, T. Inagaki, K. Asano, *Sci. Technol. Adv. Mater.* **2014**, *15*, 015009.
[40] D. Matsunami, A. Fujita, K. Takenaka, M. Kano, *Nat. Mater.* **2015**, *14*, 73.
[41] Y. You, H. Bai, X. Feng, X. Fan, L. Han, X. Zhou, Y. Zhou, R. Zhang, T. Chen, F. Pan, C. Song, *Nat. Commun.* **2021**, *12*, 6524.
[42] J. M. Taylor, A. Markou, E. Lesne, P. K. Sivakumar, C. Luo, F. Radu, P. Werner, C. Felser, S. S. P. Parkin, *Phys. Rev. B* **2020**, *101*, 094404.
[43] X. Zhou, J.-P. Hanke, W. Feng, S. Blügel, Y. Mokrousov, Y. Yao, *Phys. Rev. Mater.* **2020**, *4*, 024408.
[44] F. Johnson, J. Kimék, J. Zemen, Z. Šobén, E. Schmoranzerové, J. Godinho, P. Nemec, S. Beckert, H. Reichlové, D. Boldrin, J. Wunderlich, L. F. Cohen, *Appl. Phys. Lett.* **2022**, *120*, 232402.
[45] L. Šmejkal, J. Sinova, T. Jungwirth, *Phys. Rev. X* **2022**, *12*, 040501.
[46] P. Wadley, B. Howells, J. Železný, C. Andrews, V. Hills, R. P. Campion, V. Novék, K. Olejník, F. Maccherozzi, S. S. Dhesi, S. Y. Martin, T. Wagner, J. Wunderlich, F. Freimuth, Y. Mokrousov, J. Kuneš, J. S. Chauhan, M. J. Grzybowski, A. W. Rushforth, K. W. Edmonds, B. L. Gallagher, T. Jungwirth, *Science* **2016**, *351*, 587.
[47] X. Chen, X. Zhou, R. Cheng, C. Song, J. Zhang, Y. Wu, Y. Ba, H. Li, Y. Sun, Y. You, Y. Zhao, F. Pan, *Nat. Mater.* **2019**, *18*, 931.
[48] A. Biswas, C.-H. Yang, R. Ramesh, Y. H. Jeong, *Prog. Surf. Sci.* **2017**, *92*, 117.
[49] M. Lohmeier, E. Vlieg, *J. Appl. Crystallogr.* **1993**, *26*, 706.
[50] U. H. Zucker, E. Perenthaler, W. F. Kuhs, R. Bachmann, H. Schulz, *J. Appl. Crystallogr.* **1983**, *16*, 358.
[51] A. Ederly, *Higher Transcendental Functions*, vol. *3*, McGraw-Hill, New York **1953**.

© 2023 The Authors. Advanced Materials published by Wiley-VCH GmbH